Article

Selective Binding and Quantitation of Calcium with a Cobalt-Based Magnetic Resonance Probe

Kang Du, Agnes E. Thorarinsdottir, and T. David Harris

J. Am. Chem. Soc., **Just Accepted Manuscript** • DOI: 10.1021/jacs.9b02661 • Publication Date (Web): 04 Apr 2019

Selective Binding and Quantitation of Calcium with a Cobalt-Based Magnetic Resonance Probe

Kang Du, Agnes E. Thorarinsdottir, and T. David Harris*

Department of Chemistry, Northwestern University, Evanston, Illinois 60208-3313, United States

ABSTRACT: We report a cobalt-based paramagnetic chemical exchange saturation transfer (PARACEST) magnetic resonance (MR) probe that is able to selectively bind and quantitate the concentration of Ca^{2+} ions under physiological conditions. The parent LCo complex features CEST-active carboxamide groups and an uncoordinated crown ether moiety in close proximity to a high-spin pseudo-octahedral Co^{II} center. Addition of Na^+, Mg^{2+}, K^+, and Ca^{2+} leads to binding of these metal ions within the crown ether. Single-crystal X-ray diffraction and solid-state magnetic measurements reveal the presence of a cation-specific coordination environment and magnetic anisotropy of Co^{II}, with axial zero-field splitting parameters for the Na^+- and Ca^{2+}-bound complexes differing by over 90%. Owing to these differences, solution-based measurements under physiological conditions indicate reversible binding of Na^+ and Ca^{2+} to give well-separated CEST peaks at 69 and 80 ppm for $[LCoNa]^+$ and $[LCoCa]^{2+}$, respectively. Dissociation constants for different cation-bound complexes of LCo, as determined by ^1H NMR spectroscopy, demonstrate high selectivity toward Ca^{2+}. This finding, in conjunction with the large excess of Na^+ in physiological environments, minimizes interference from related cations, such as Mg^{2+} and K^+. Finally, variable-$[Ca^{2+}]$ CEST spectra establish the ratio between the CEST peak intensities for the Ca^{2+}- and Na^+-bound probes ($CEST_{80\ ppm}/CEST_{69\ ppm}$) as a measure of $[Ca^{2+}]$, providing the first example of a ratiometric quantitation of Ca^{2+} concentration using PARACEST. Taken together, these results demonstrate the ability of transition metal PARACEST probes to afford a concentration-independent measure of $[Ca^{2+}]$, and provide a new approach for designing MR probes for cation sensing.

INTRODUCTION

The concentration of Ca^{2+} ions in blood serum is a vital biomarker for bone-related diseases, such as cancer,[1] hyperparathyroidism,[2] and Paget's disease.[3] These diseases are associated with the dissolution of bone tissue, which releases Ca^{2+} into the blood stream and results in hypercalcemia, a medical condition where the total Ca^{2+} concentration in serum exceeds 2.6 mM.[4] In current clinical settings, the presence and extent of hypercalcemia is evaluated by blood tests. This form of analysis provides only an estimate of the total Ca^{2+} concentration in serum, with no information on the spatial distribution or local concentration of Ca^{2+} near the bone lesion. As such, while blood tests can conveniently confirm the presence of hypercalcemia, they do not enable an assessment of the underlying source and cause of high Ca^{2+} concentrations.[5] For these reasons, realization of an imaging technique able to quantitate the local Ca^{2+} concentration near bone tissue would be highly useful in the early detection of bone-related diseases and in pathological studies.

Magnetic resonance imaging (MRI) is a non-invasive technique that is particularly well suited for measuring the concentration of Ca^{2+} near bone tissue owing to its unlimited depth penetration of tissue and its ability to provide spatiotemporal images.[6] Toward this end, several Gd^{III}-based probes have been developed to detect Ca^{2+} ions by virtue of relaxivity changes upon binding Ca^{2+}.[7] Here, extensive synthetic modifications have been employed to impart selective binding of Ca^{2+} in the presence of other cations.[7] Nevertheless, the utility of these probes is limited by heterogeneous biodistribution of Ca^{2+} and/or the probes themselves. It is therefore critical to develop MRI probes capable of selectively binding and quantitating Ca^{2+} through a concentration-independent method.

Lanthanide-[8] and transition metal-based[9] paramagnetic chemical exchange saturation transfer (PARACEST) probes, which deliver magnetization to bulk H_2O through chemical exchange of protons, have been reported to detect a number of biomarkers, such as redox environment,[10] pH,[9e,11] temperature,[12] and Zn^{2+} ions.[13] The exchangeable proton resonances, commonly from coordinating H_2O, carboxamides, and nitrogen heterocycles, are paramagnetically shifted, thus minimizing interference from labile protons in biological systems. Furthermore, the large chemical shifts allow for faster proton exchange, hence more pronounced contrast can be realized. The frequency-specific contrast afforded by PARACEST probes enables simultaneous detection of more than one CEST peak. As a result, the intensity ratio of two distinct CEST peaks that exhibit different responses can provide an effective and concentration-independent measure of biomarkers.[8b,9e,10c,11a,b,d–f,h,j,k]

An ideal Ca^{2+}-responsive PARACEST probe should feature a recognition moiety that is moderately selective for Ca^{2+},[8e] yet can reversibly bind other cations of concentrations that are relatively constant in serum, in order to enable a ratiometric measurement. One such cation is Na^+, which exhibits a relatively constant concentration of ca. 140 mM in serum.[14] In addition, the frequencies of CEST peaks for Ca^{2+}- and Na^+-bound complexes should be well separated to avoid interference, analogously to the attributes of a ^{19}F probe.[15] Along these lines, alkali and alkaline earth cations have been shown to significantly influence the magnetic anisotropy of a nearby paramagnetic metal ion, by causing distortions in the local coordination environment.[16] Because the proton hyperfine shift is highly sensitive to changes in metal coordination environment and magnetic anisotropy,[17] the CEST peak frequency can be indicative of the identity of the bound cation. As such, we set out to design a probe that features (1) a cation binding moiety with proper affinities toward Ca^{2+} and Na^+ to allow for an equilibrium between the Ca^{2+}- and Na^+-bound probes under physiological conditions, (2) a paramagnetic center with magnetic properties and coordination environment that is highly sensitive toward the identities of cations within its vicinity, and (3) a functional group capable of producing CEST effects.

A high-magnetic anisotropy Co^{II} complex that features coordinated carboxamide ligands and a proximate crown ether satisfies

all of these criteria. Encouragingly, complexes of a Schiff base-18-crown-6 dinucleating ligand have recently been employed to modulate the electronic structure of Co^{II} via cation complexation.[18] Herein, we present a Co^{II}-based PARACEST probe that can reversibly bind Ca^{2+} and Na^{+} under physiological conditions. The ratio of CEST signal intensities from the resulting Ca^{2+}- and Na^{+}-bound probes enables, for the first time, the concentration-independent quantitation of Ca^{2+} concentration by a MR-based method.

EXPERIMENTAL SECTION

General Considerations. Unless otherwise specified, chemicals and solvents were purchased from commercial vendors and used without further purification. Deuterated solvents were purchased from Cambridge Isotope Laboratories. When necessary for moisture sensitive experiments, glassware was flame dried or stored in an oven at 150 °C for at least 4 h, followed by cooling in a desiccator. Air- and water-free manipulations were carried out in a Vacuum Atmosphere Nexus II glovebox or using standard Schlenk techniques under a dry dinitrogen atmosphere. Air-free experiments involving the use of water were carried out in an MBraun LABstar glovebox under a humid dinitrogen atmosphere. Acetonitrile (MeCN), diethyl ether (Et_2O), and methanol (MeOH) were dried using a commercial solvent purification system from Pure Process Technology. MeCN was stored over 4 Å molecular sieves prior to use. Water was obtained from a purification system from EMD Millipore. Experimental details on the syntheses of organic ligand precursors are provided in the Supporting Information.

Synthesis of 2,2′-(1²,8²-dihydroxy-9,12,15,18-tetraoxa-3,6-diaza-1,8(1,3)-dibenzenacyclooctadecaphane-3,6-diyl)diacetamide (H_2L, see Scheme S1). Under a dry dinitrogen atmosphere, 13,16,19,22-tetraoxa-3,6-diazatricyclo[21.3.1.1^{8,12}]octacosa-1(27),8,10,12(28),23,25-hexaene-27,28-diol (0.20 g, 0.48 mmol) and diisopropylethylamine (0.12 g, 0.96 mmol) were dissolved in MeCN (20 mL) to give a brown solution. The solution was heated at reflux and 2-bromoacetamide (0.13 g, 0.96 mmol) was added dropwise to the boiling solution with vigorous stirring. After stirring at reflux for 12 h, basic alumina (2 g) was added and the mixture was evaporated to dryness under reduced pressure. The resulting powder was dry-loaded on a basic alumina column, which was packed using CH_2Cl_2 eluent. After loading, the column was first eluted with 2% (v/v) MeOH/CH_2Cl_2 until no compound was detected by thin-layer chromatography (TLC), as visualized by I_2 vapor, to remove an impurity (R_f = 0.6 in 5% (v/v) MeOH/CH_2Cl_2). The column was then eluted with 5% (v/v) MeOH/CH_2Cl_2 to obtain the desired product (R_f = 0.3 in 5% (v/v) MeOH/CH_2Cl_2). The combined fractions were evaporated to dryness under reduced pressure to give the product as an off-white solid (25 mg, 10%). ^{1}H NMR (MeOH-d_4): 6.88 (t, 2H), 6.72 (m, 4H), 4.14 (m, 4H), 3.88 (m, 4H), 3.77 (s, 4H), 3.65 (s, 4H), 3.03 (s, 4H), 2.72 (s, 4H).

Synthesis of LCo·3.1H₂O (**1**, see Figure 1). Under a dinitrogen atmosphere, H_2L (25 mg, 0.047 mmol) was dissolved in MeOH (5 mL). To this colorless solution, a solution of $Co(CH_3COO)_2{\cdot}4H_2O$ (12 mg, 0.048 mmol) in MeOH (5 mL) was added. The resulting light magenta solution was heated at reflux under a dinitrogen atmosphere for 12 h. The solution was evaporated to dryness and the residue was dissolved in MeOH (2 mL). The pink solution was added to Et_2O (15 mL) with vigorous stirring, to induce the formation of a pink precipitate. The pink solid was collected by filtration, washed with Et_2O (5 mL), and dried in vacuo for 20 h to give **1** (25 mg, 82%). Anal. Calcd. for $C_{26}H_{40.2}CoN_4O_{11.1}$: C, 48.4; H, 6.28; N, 8.68. Found: C, 48.2; H, 5.62; N, 9.14. UV-visible absorption spectrum (H_2O, 25 °C): 517 nm (ε = 59.5 M^{-1} cm^{-1}), 526 nm (ε = 57.7 M^{-1} cm^{-1}). FT-IR (ATR, cm^{-1}): 3341 (s, broad); 2916 (m); 2872 (m); 1662 (s); 1589 (s); 1562 (s); 1456 (s); 1304 (m); 1229 (s); 1110 (s); 1070 (s); 987 (m); 955 (m); 932 (m); 894 (m); 840 (m); 737 (s); 587 (w); 439 (w); 407 (w). Solution magnetic moment (D_2O, 37 °C): $\chi_M T$ = 2.4(3) cm^3 K mol^{-1}. Slow diffusion of acetone into a pink solution of **1** in H_2O over two weeks yielded single crystals of $LCo{\cdot}0.50C_3H_6O{\cdot}9.05H_2O$ (**1′**) suitable for X-ray structural analysis.

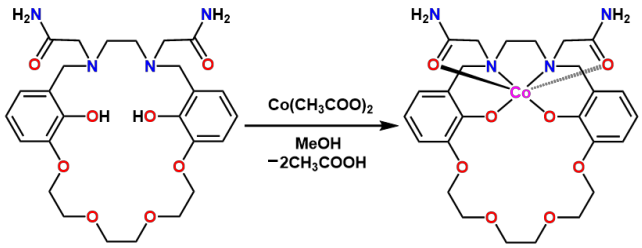

Figure 1. Synthesis and molecular structure of LCo.

Synthesis of LCoNa(NO₃)·1.7H₂O (**2**). To a stirring pink solution of **1** (30 mg, 0.046 mmol) in MeOH (5 mL), a solution of $NaNO_3$ (4.3 mg, 0.051 mmol) in MeOH (0.5 mL) was added. The resulting pink solution was stirred for 5 min at ambient temperature and then filtered through diatomaceous earth. Slow diffusion of Et_2O into the pink solution over three days resulted in pink crystalline solid, which was collected by filtration and dried in vacuo for 20 h to afford **2** (34 mg, 95%). Anal. Calcd. for $C_{26}H_{37.4}CoN_5NaO_{12.7}$: C, 44.3; H, 5.35; N, 9.93. Found: C, 44.3; H, 5.16; N, 10.1. FT-IR (ATR, cm^{-1}): 3356 (s, broad); 2921 (m); 2873 (m); 1666 (s); 1591 (m); 1564 (m); 1476 (s); 1458 (s); 1302 (m); 1270 (m); 1231 (s); 1107 (s); 1086 (s); 987 (m); 956 (m); 930 (m); 896 (m); 840 (m); 741 (s); 409 (m). Slow diffusion of acetone into a pink solution of **2** in H_2O over two weeks yielded single crystals of $[LCoNa(H_2O)](NO_3)_{0.5}(OH)_{0.5}{\cdot}5.8H_2O$ (**2′**) suitable for X-ray structural analysis.

Synthesis of LCoCa(NO₃)₂·0.25Et₂O·0.50H₂O (**3**). To a stirring pink solution of **1** (30 mg, 0.046 mmol) in MeOH (5 mL), a solution of $Ca(NO_3)_2{\cdot}4H_2O$ (12 mg, 0.051 mmol) in H_2O (0.5 mL) was added. The resulting pink solution was stirred for 5 min at ambient temperature and then filtered through diatomaceous earth. Slow diffusion of Et_2O into the pink solution over four days resulted in pink crystalline solid, which was collected by filtration and dried in vacuo for 20 h to afford **3** (30 mg, 83%). Anal. Calcd. for $C_{27}H_{37.5}CaCoN_6O_{14.75}$: C, 41.5; H, 4.84; N, 10.8. Found: C, 41.5; H, 5.03; N, 10.9. FT-IR (ATR, cm^{-1}): 3341 (s, broad); 2922 (m); 2874 (m); 1662 (s); 1600 (m); 1566 (m); 1475 (s); 1325 (s); 1303 (m); 1233 (s); 1105 (s); 1086 (s); 1071 (s); 1022 (m); 983 (m); 958 (m); 942 (m); 843 (m); 828 (m); 738 (s); 444 (w); 431 (m). Slow diffusion of Et_2O into a pink solution of **3** in MeOH over two weeks yielded single crystals of $[LCoCa(NO_3)(MeOH)](NO_3){\cdot}MeOH$ (**3′**) suitable for X-ray structural analysis.

X-Ray Structure Determination. Single crystals of **1′**, **2′**, and **3′** were directly coated with Paratone-N oil and mounted on a MicroMounts™ rod. The crystallographic data were collected at 100 K on a Bruker APEX II diffractometer equipped with a MoKα sealed tube source. Raw data were integrated and corrected for Lorentz and polarization effects using Bruker APEX2 v. 2009.1.[19] The program SADABS was used to apply absorption correction.[20] Space group assignments were determined by examining systematic absences, E-statistics, and successive refinement of the structure. Structures were solved by SHELXT[21a,b] using direct methods and refined by SHELXL[21a,b] within the OLEX2 interface.[21c] All hydrogen atoms were placed at calculated positions using suitable riding models and refined using isotropic displacement parameters derived from their parent atoms. Thermal parameters for all non-hydrogen atoms were refined anisotropically. The solvent mask procedure as implemented in OLEX2 was applied to the structures of **1′** and **2′** to account for severely disordered solvent molecules that could not be properly modeled. Void volumes of 9484.8 and 11161.8 Å^3 with a total of 4060.8 and 3043.0 electrons, respectively, were found per unit cell in the crystal structures of **1′** and **2′**,

respectively. These were ascribed to 8.5 and 6.3 H_2O molecules per LCo unit in the structures of **1′** and **2′**, respectively. In the structure of **2′**, the occupancies of Na^+ and NO_3^- ions within each asymmetric unit were found to be 1.0 and 0.5, respectively. As such, 0.5 OH^- ion per LCo unit is likely present for charge balancing. Crystallographic data for **1′**, **2′**, and **3′** at 100 K and the details of data collection are listed in Tables S1–S3.

Solid-State Magnetic Measurements. Magnetic measurements of **1**, **2**, and **3** were performed on polycrystalline samples dispensed in icosane. Samples were loaded in quartz tubes under a dinitrogen atmosphere, attached to a sealable hose adapter, and flame sealed under vacuum on a Schlenk manifold. All data were collected using a Quantum Design MPMS-XL SQUID magnetometer. The reduced magnetization data were collected between 1.8 and 10 K at applied dc fields ranging from 0 to +7 T. The program PHI[22] was employed to simulate the reduced magnetization data using the following spin Hamiltonian:

$$\hat{H} = D\hat{S}_z^2 + g\mu_B \boldsymbol{S}\cdot\boldsymbol{H} \quad (1)$$

In this Hamiltonian, D is the axial zero-field splitting parameter, $\hat{S}_z$ is the z component of the spin angular momentum operator, g is the electron spin g-factor, μ_B is the Bohr magneton, $\boldsymbol{S}$ is the spin angular momentum, and $\boldsymbol{H}$ is the applied magnetic field. Isotropic g values of 2.30(1), 2.28(1), and 2.33(1) were used for fitting the data for **1**, **2**, and **3**, respectively, to extract the D values (see Table 1 and Figure 2).

Solution Magnetic Measurements. The solution magnetic moment of **1** was determined at 37 °C using the Evans method[23] by collecting ^{1}H NMR spectra on an Agilent DD2 500 MHz (11.7 T) system. Samples contained 5 mM of **1** in a mixture of 0.5% (w/w) of dimethyl sulfoxide (DMSO) in D_2O and were prepared under dinitrogen atmosphere to ensure no degradation due to oxidation by air. A capillary containing the same solvent mixture but without **1** was inserted into each NMR sample tube as a reference. Diamagnetic corrections were carried out based on the empirical formula of **1** using Pascal's constants.[24] The paramagnetic molar susceptibility χ_M^{para} ($cm^3\ mol^{-1}$) was calculated using the following equation:[23]

$$\chi_M^{para} = (3\Delta\nu M_w)/(4\pi\nu_0 m) - \chi_M^{dia} \quad (2)$$

In this equation, $\Delta\nu$ is the frequency difference (Hz) between the DMSO resonance in the sample and reference solutions, M_w is the molecular mass of the paramagnetic compound (g mol^{-1}), ν_0 is the operating frequency of the NMR spectrometer (Hz), m is the concentration of the paramagnetic compound (g cm^{-3}), and χ_M^{dia} is the diamagnetic contribution to the molar susceptibility ($cm^3\ mol^{-1}$). The reported value of $\chi_M T$ is an average from three independent measurements.

^{1}H NMR Spectroscopy. ^{1}H NMR spectra of H_2L and ligand precursors were collected at 25 °C on an automated Agilent DD MR 400 MHz (9.4 T), an Agilent DD2 500 MHz (11.7 T), or on a Varian Inova 500 MHz (11.7 T) spectrometers. All ^{1}H NMR spectra of cobalt complexes were recorded at 37 °C. Data for dissociation constant (K_d) measurements in D_2O were collected on a Bruker Avance III HD Nanobay 400 MHz (9.4 T) system (for Na^+ and K^+) or on a Bruker Neo 600 MHz (14.1 T) system equipped with a QCI-F cryoprobe (for Mg^{2+} and Ca^{2+}), and data for K_d measurements in 50 mM 4-(2-hydroxyethyl)-1-piperazineethanesulfonic acid (HEPES) buffer solutions at pH 7.3–7.5 were collected on an Agilent DD2 500 MHz (11.7 T) system. ^{1}H NMR spectra of samples of **1** in D_2O and in 50 mM HEPES buffer solutions at pH 7.4 were collected on a Bruker Avance III HD Nanobay 400 MHz (9.4 T) system and on an Agilent DD2 500 MHz (11.7 T) system, respectively. For the HEPES buffer solution samples, D_2O was placed in an inner capillary within each NMR sample tube to lock the sample. Samples were prepared and stored under dinitrogen atmosphere to ensure no degradation due to oxidation by air. Note that the pH of the buffer solutions was adjusted to the desired values using aqueous HCl and NMe_4OH solutions to avoid introduction of inorganic cations. Chemical shift values (δ) are reported in ppm and referenced to residual signals from the deuterated solvents (7.26 ppm for $CDCl_3$, 3.31 ppm for MeOH-d_4, and 2.50 ppm for DMSO-d_6). For measurements of complexes in D_2O or H_2O, the chemical shift of the solvent signal was set to 0 ppm to simplify comparison between ^{1}H NMR and CEST spectra (see Figures S1 and S2).

CEST Experiments. All CEST experiments were performed at 37 °C on an Agilent DD2 500 MHz (11.7 T) or a Varian Inova 500 MHz (11.7 T) systems. Samples for measurements contained 2.5–11 mM of **1** in 50 mM HEPES buffer solutions at pH 7.4, in the absence and presence of inorganic cations. All samples were prepared and stored under dinitrogen atmosphere to ensure no degradation due to oxidation by air. Z-spectra (CEST spectra) were obtained according to the following protocol. ^{1}H NMR spectra were acquired from −100 to 100 ppm frequency offset (chemical shift with respect to the bulk H_2O signal) with a step increase of 1 ppm using a presaturation pulse applied for 3 s at a power level (B_1) of 21–22 μT. The B_1 values were calculated based on the calibrated 90° pulse on a linear amplifier. D_2O was placed in an inner capillary within each NMR sample tube to lock the sample. The obtained ^{1}H NMR spectra were plotted as normalized integrations of the H_2O signal against frequency offset to produce a Z-spectrum. Direct saturation of the H_2O signal was set to 0 ppm. CEST peak intensities from 20 to 40 ppm were fitted using a linear model to construct baselines, based on which the relevant CEST intensities were corrected. Exchange rate constants were calculated based on a reported method.[25] In particular, ^{1}H NMR spectra were acquired at various presaturation power levels ranging from 7.4 to 21 μT applied for 6 s at 37 °C.

Determination of Dissociation Constants (K_d) by ^{1}H NMR Titration Experiments. ^{1}H NMR titration experiments were performed following modified literature procedures.[26] In order to obtain accurate chemical shift and peak integration values, samples were prepared in D_2O under dinitrogen atmosphere. Reported values of K_d for each cation-bound complex are averages from two independent experiments. For $[LCoM]^{+/2+}$ ($M^{+/2+} = Na^+, Mg^{2+}, K^+$), values of K_d were estimated by monitoring changes in ^{1}H NMR chemical shift for two different resonances (see Table S4) and averages from these data sets are reported in Table 2. To estimate K_d for the interaction between LCo and Na^+ and Mg^{2+} ions, samples containing 2.5 or 1.0 mM of **1** were mixed with various amounts of $NaNO_3$ or $Mg(NO_3)_2$ to give final concentrations of Na^+ and Mg^{2+} ranging from 0 to 18.7 mM and 0 to 56.7 mM, respectively. The interconversion rate between $\{LCo + M^{+/2+}\}$ and $[LCoM]^{+/2+}$ ($M^{+/2+} = Na^+, Mg^{2+}$) was fast compared to the ^{1}H NMR acquisition time scale (ca. 10^{-3} s), as evidenced by the presence of a single set of NMR resonances for the whole series of spectra for both ions. The changes in chemical shift ($\Delta\delta$) for the peaks at ca. 202 and 123 ppm were monitored for each added ion (see Figures 3, left, and S3–S5) and fitted using the program Dynafit[27] to extract values of K_d (see Script S1, and Tables 2 and S4). Representative fits of these data are shown in Figures S6–S9.

Because K_d for $[LCoK]^+$ was expected to be lower than that for $[LCoNa]^+$, 150 mM of Na^+ was introduced to compete with K^+ for binding to LCo, so an equilibrium could be established at a concentration of **1** high enough to be observed by ^{1}H NMR. Samples containing 2.5 mM of **1** and 150 mM of $NaNO_3$ in D_2O were mixed with various amounts of KNO_3 to give final concentrations of K^+ ranging from 0 to 18.6 mM. The interconversion rate between $\{[LCoNa]^+ + K^+\}$ and $\{[LCoK]^+ + Na^+\}$ was fast compared to the ^{1}H NMR acquisition time scale (ca. 10^{-3} s), as evidenced by the presence of a single set of NMR resonances for the series of spectra. The changes in chemical shift ($\Delta\delta$) for the peaks at ca. 212 and 133 ppm (see Figures S10 and S11) were fitted using Dynafit,[27] using a

competition model (see Script S2), to afford values of K_d (see Figures S12 and S13, and Tables 2 and S4).

To determine K_d for $[LCoCa]^{2+}$, K^+ was used as a competing ion. Samples containing 1.0 mM of **1** and 30 mM of KNO_3 were mixed with various amounts of $Ca(NO_3)_2$ to give final concentrations of Ca^{2+} ranging from 0 to 3.65 mM. The increase in the intensity of the peak at 245 ppm with increasing concentration of Ca^{2+} and the concomitant decrease in signal intensity for the peak at 207 ppm indicated a slow interconversion rate between $\{[LCoK]^+ + Ca^{2+}\}$ and $\{[LCoCa]^{2+} + K^+\}$ compared to the ^1H NMR acquisition time scale (ca. 10^{-3} s). The integration values for the peaks at 207 and 245 ppm were normalized to represent the relative percentages of $[LCoK]^+$ and $[LCoCa]^{2+}$ in the samples (see Figure S14). The value of K_d for $[LCoCa]^{2+}$ was estimated using the following equation (see Table 2):

$$K_{d\ (LCoCa)} = K_{d\ (LCoK)} \times [Ca^{2+}]/[K^+] \quad (3)$$

In this equation, $K_{d\ (LCoK)}$ is the average K_d value obtained for $[LCoK]^+$, and $[Ca^{2+}]$ and $[K^+]$ are the concentrations of free Ca^{2+} and K^+ ions when $[LCoK]^+ : [LCoCa]^{2+} = 1 : 1$.

To investigate the effects of pH on cation binding to LCo and compare to the data obtained in D_2O, ^1H NMR titration experiments were repeated for Na^+ in deoxygenated 50 mM HEPES buffer solutions at pH 7.3–7.5. Samples containing 5.0 mM of **1** and 50 mM of HEPES buffered at pH 7.3, 7.4, and 7.5, respectively, were mixed with various amounts of $NaNO_3$ to give final concentrations of Na^+ ranging from 0 to 18.2 mM. The change in chemical shift ($\Delta\delta$) for the peak at ca. 123 ppm was monitored and fitted using a non-competition model in Dynafit[27] (see Script S1) to obtain values of K_d as described above. These data are summarized in Figures S15–S17 and Table S5.

Electrochemical Measurements. Cyclic voltammetry measurements were carried out in a standard one-compartment cell using CH Instruments 760 c potentiostat under a humid dinitrogen atmosphere inside an MBraun LABstar glovebox at ambient temperature. The cell consisted of a glassy carbon electrode as a working electrode, a platinum wire as a counter electrode, and a saturated calomel electrode (SCE) as a reference electrode. The analyte solutions were prepared using 50 mM of HEPES buffered at pH 7.4 with either 100 mM of NMe_4Cl or a mixture of inorganic cations at their physiological concentrations (150 mM of NaCl, 4 mM of KNO_3, 2 mM of $Ca(NO_3)_2$, and 0.2 mM of $Mg(NO_3)_2$) as an electrolyte. The voltammograms were converted and referenced to the normal hydrogen electrode (NHE), using a literature conversion factor.[28]

Other Physical Measurements. Infrared data were collected on a Bruker Alpha FTIR spectrometer equipped with an attenuated total reflectance accessory. Solution UV-visible-NIR spectra were obtained using an Agilent Cary 5000 spectrophotometer. Elemental analyses of **1**, **2**, and **3** were performed by Midwest Microlab (Indianapolis, IN).

RESULTS AND DISCUSSION

Syntheses and Structures. The design of H_2L was inspired by previous reports of transition metal Schiff base complexes featuring an appended crown ether pocket.[16a,18,29] An S_N2 reaction between 2-bromoacetamide and a reduced salen precursor afforded H_2L (see Scheme S1). The crown ether group is responsible for cation recognition, whereas the hexadentate chelating fragment features exchangeable carboxamide protons and accommodates an anisotropic metal center suitable for PARACEST. Co^{II} is an ideal metal ion for these purposes owing to high magnetic anisotropy and fast electronic relaxation time.[17] The crown ether moiety was expected to be well suited for selective and reversible binding of Ca^{2+} under physiological conditions as it mimics the organic molecule 18-crown-6, which is well known to bind cations with different affinities based on their size and charge.[30] Furthermore, structural changes in the crown ether pocket caused by cation binding were

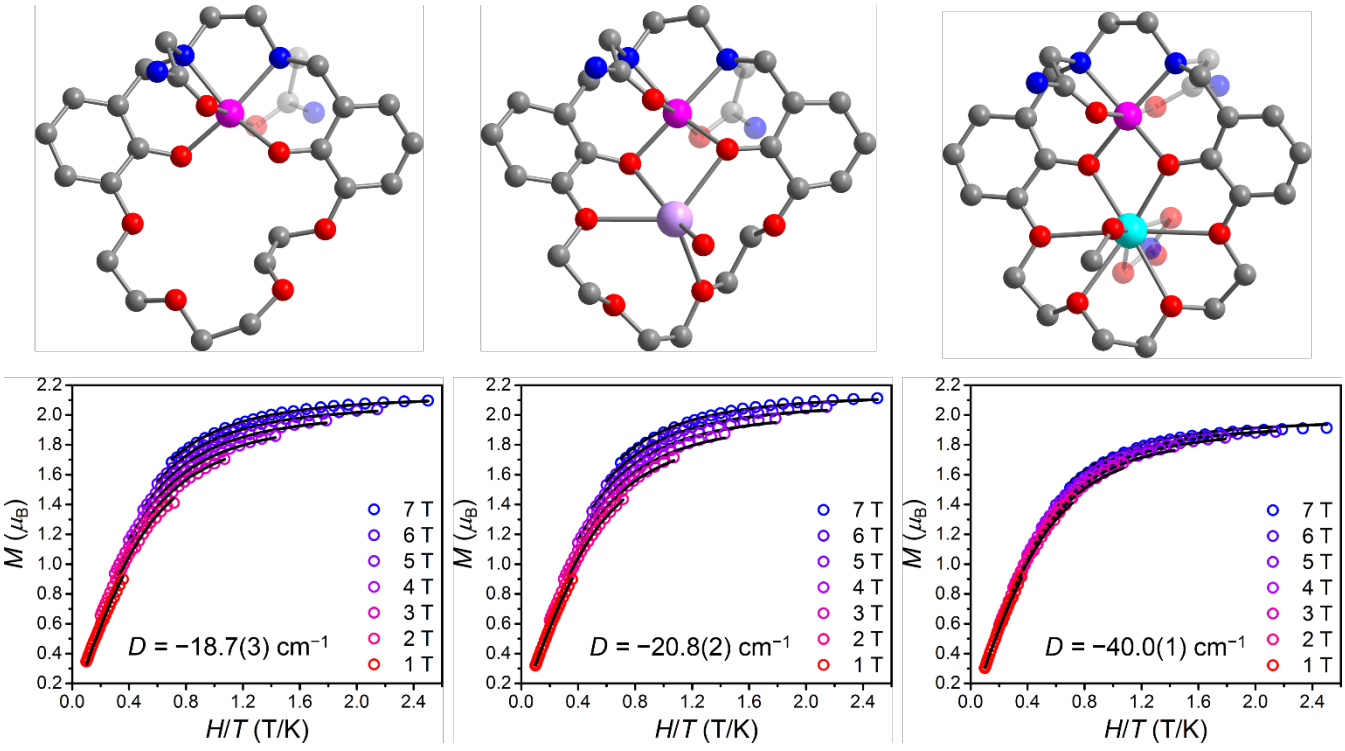

Figure 2. Upper: Crystal structures of LCo (left), $[LCoNa(H_2O)]^+$ (middle), and $[LCoCa(NO_3)(MeOH)]^+$ (right), as observed in **1′**, **2′**, and **3′**, respectively. Magenta, cyan, lilac, red, blue, and gray spheres represent Co, Ca, Na, O, N, and C atoms, respectively; H atoms are omitted for clarity. Lower: Low-temperature magnetization data for **1** (left), **2** (middle), and **3** (right), collected at selected dc fields (see legends). Colored circles and black solid lines represent experimental data and corresponding fits, respectively.

Table 1. Selected mean interatomic distances and octahedral distortion parameter (Σ)[31] for **1′**–**3′**, and axial zero-field splitting parameter (D) for **1**–**3**.

	1′ / 1	**2′ / 2**	**3′ / 3**
Co–O_{amide} (Å)	2.158(4)	2.15(3)	2.12(3)
Co–$O_{phenoxo}$ (Å)	2.00(2)	2.009(8)	1.978(1)
Co–N (Å)	2.22(3)	2.18(3)	2.141(5)
Σ(°)	97.8(5)	91.6(4)	66.3(2)
D (cm^{-1})	−18.7(3)	−20.8(2)	−40.0(1)

envisioned to influence the coordination geometry of the hexadentate chelate, and thus affect the magnetic anisotropy of the paramagnetic Co^{II} center. These changes in magnetic anisotropy of Co^{II} were anticipated to impact the hyperfine shifts of carboxamide protons from the pendent donors, providing CEST peaks with cation-dependent frequencies.

Reaction of H_2L with $Co(CH_3COO)_2{\cdot}4H_2O$[16a,18,29] afforded the pink compound $LCo{\cdot}3.1H_2O$ (**1**) in 82% yield (see Figure 1). Subsequent addition of stoichiometric amounts of $NaNO_3$ or $Ca(NO_3)_2{\cdot}4H_2O$ yielded the compounds $LCoNa(NO_3){\cdot}1.7H_2O$ (**2**) or $LCoCa(NO_3)_2{\cdot}0.25Et_2O{\cdot}0.50H_2O$ (**3**), respectively. Slow diffusion of acetone into aqueous solutions of **1** or **2**, or Et_2O into a solution of **3** in MeOH, gave pink block-shaped crystals of $LCo{\cdot}0.50C_3H_6O{\cdot}9.05H_2O$ (**1′**), $[LCoNa(H_2O)](NO_3)_{0.5}(OH)_{0.5}{\cdot}5.8H_2O$ (**2′**), and $[LCoCa(NO_3)(MeOH)](NO_3){\cdot}MeOH$ (**3′**), respectively. Single-crystal X-ray diffraction analyses of **1′**–**3′** (see Tables S1–S3) revealed that the Co^{II} ion resides in a distorted octahedral environment in all three structures, with the N_2O_2 pocket of L^{2-} comprising the equatorial plane and the O atoms from the pendent carboxamide groups coordinating the axial sites (see Figure 2, upper). In **2′**, a Na^+ ion is ligated by four of the six O atoms from the crown ether unit of L^{2-} and a H_2O molecule to give an irregular five-coordinate complex. In stark contrast, **3′** features a nine-coordinate Ca^{2+} ion that induces only a minimal distortion to the crown ether, where all six Ca–O_{crown} distances are shorter than 2.74 Å. The remaining three coordination sites of Ca^{2+} are occupied by a MeOH molecule and an η^2-NO_3^- ion. Because Ca^{2+} and Na^+ have similar ionic radii,[31] the less distorted structure in **3′** than **2′** likely stems from greater electrostatic attraction between Ca^{2+} and the O atoms.

The conformational differences between the crown ether units in **1′**, **2′**, and **3′** caused significant structural differences at the Co^{II} center in the three compounds. This effect can be quantified through the octahedral distortion parameter (Σ), which is defined as the sum of the absolute deviations from 90° for all 12 *cis* L–Co–L angles.[32] Across the series, **1′** features the largest distortion from an octahedral geometry at Co^{II} with Σ = 97.8(5)°, followed by **2′** with Σ = 91.6(4)°, and **3′** with Σ = 66.3(2)° (see Table 1).

Solid-State Magnetic Properties. Given the significant differences in coordination geometry at Co^{II} across the three compounds, one would expect associated changes in magnetic anisotropy. To probe the influence of coordination geometry on magnetic anisotropy in these compounds, low-temperature magnetization data were collected for polycrystalline samples of **1**, **2**, and **3** at selected dc fields (see Figure 2, lower). The non-superimposability of the resulting isofield curves for all compounds, along with their saturation magnetization values below M = 3 μ_B expected for an isotropic $S = {}^3/_2$ Co^{II} center, indicates the presence of significant zero-field splitting, which is a measure of magnetic anisotropy. This effect was quantified by fitting the data using equation 1 (see Experimental Section),[22] giving axial zero-field splitting parameters of D = −18.7(3), −20.8(2), and −40.0(1) cm^{-1} for **1**, **2**, and **3**, respectively. Here, the magnitude of D increases with decreasing distortion from octahedral geometry at Co^{II}, which is in line with a progression toward orbital degeneracy in moving from **1** to **2** to **3**.

Solution ^{1}H NMR Properties. To probe how changes in magnetic anisotropy of Co^{II} affect the NMR hyperfine shifts of ligand protons in **1**, **2**, and **3**, ^{1}H NMR spectra were collected at 37 °C for solutions containing 5 mM of **1** and 50 mM of HEPES buffered at pH 7.4, in the absence and presence of 15 mM of $NaNO_3$ or $Ca(NO_3)_2$. Note that excess amounts of Na^+ and Ca^{2+} were used to ensure complete cation binding, and no further spectral changes were observed beyond this concentration. Spectra for all three solutions display sharp peaks spanning from −23 to 245 ppm vs H_2O, consistent with high-spin Co^{II} in all compounds (see Figure S1). Carboxamide resonances were observed at 77, 69, and 80 ppm for

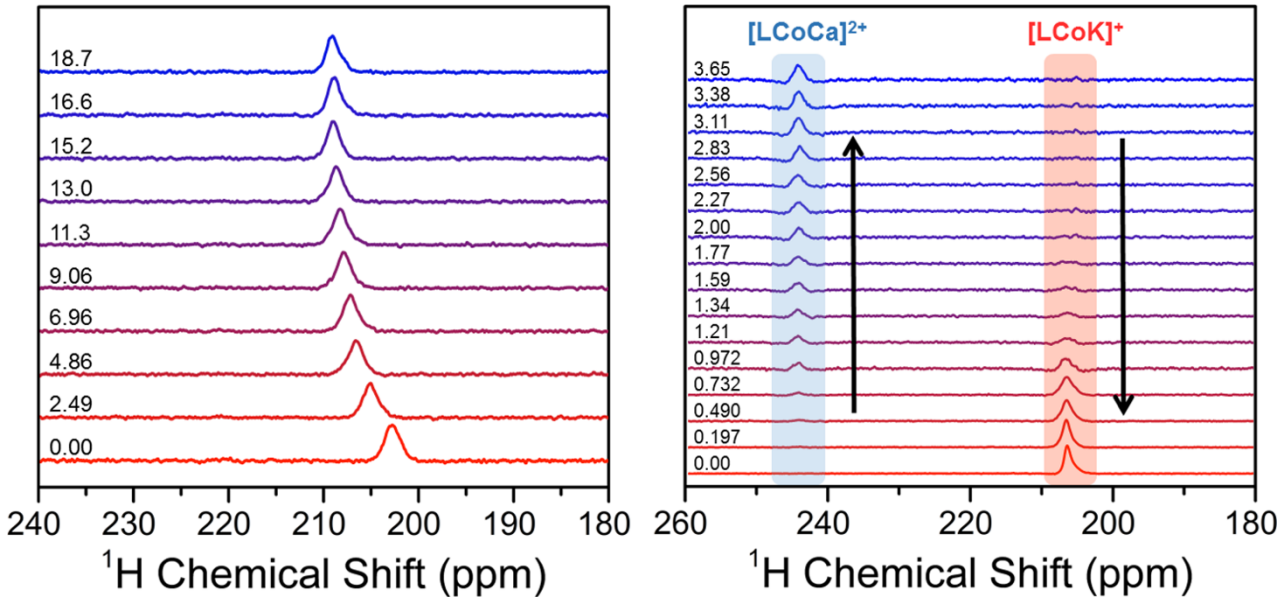

Figure 3. Left: Change in ^{1}H NMR chemical shift of a selected resonance for a 2.5 mM solution of **1** in D_2O upon incremental addition of $NaNO_3$. Right: Changes in ^{1}H NMR signal intensities of selected resonances for a D_2O solution containing 1.0 mM of **1** and 30 mM of KNO_3 upon incremental addition of $Ca(NO_3)_2$. The resonances at 207 and 245 ppm correspond to $[LCoK]^+$ and $[LCoCa]^{2+}$, respectively. Data were collected at 37 °C at 9.4 and 14.1 T for Na^+ and Ca^{2+}, respectively. Numbers next to spectra denote the concentrations of respective added cations (mM).

Table 2. Summary of dissociation constants (K_d) for cation-bound complexes of **1** in D_2O at 37 °C.

	$[LCoNa]^+$	$[LCoMg]^{2+}$	$[LCoK]^+$	$[LCoCa]^{2+}$
K_d (mM)	4.8(3)[a]	23(2)[a]	0.3(2)[a]	0. 01(1)[b]

[a] Average value from monitoring ^1H NMR chemical shift changes upon cation addition for two different resonances. [b] Estimated by a method described in the Experimental Section.

1, $[LCoNa]^+$, and $[LCoCa]^{2+}$, respectively, as evidenced by their disappearance in the spectra recorded in D_2O (see Figure S2). The observation of a single carboxamide peak for all compounds suggests chemical equivalence of the two carboxamide groups in each molecule. Importantly, the difference in chemical shift of 11 ppm between the Ca^{2+}- and Na^+-bound compounds is more than two orders of magnitude greater than that of a diamagnetic analogue,[18] highlighting the high sensitivity of ^1H NMR hyperfine shift toward structural and magnetic differences at Co^{II}. Note that the carboxamide peak is not the most shifted resonance for any of the three compounds. The most shifted resonances for **1**, $[LCoNa]^+$, and $[LCoCa]^{2+}$ are located at 203, 210, and 245 ppm, respectively. The increase in maximum hyperfine shift in moving from **1** to $[LCoNa]^+$ to $[LCoCa]^{2+}$ is in good agreement with the increase in magnetic anisotropy across the series, as evident from solid-state magnetic measurements. The 35 ppm difference in maximum hyperfine shift between $[LCoCa]^{2+}$ and $[LCoNa]^+$ represents even higher cation sensitivity, suggesting that there is a large room for improving the sensitivity of cation-sensing MR probes.

Assessment of Cation Binding Affinities by ^1H NMR. While UV-visible absorption spectroscopy is commonly used to determine dissociation constants, the UV-visible spectra for aqueous solutions of **1**, $[LCoNa]^+$, and $[LCoCa]^{2+}$ reveal no significant differences (see Figure S18). However, because notable changes were observed between the ^1H NMR spectra for these compounds, and ^1H NMR has been employed in studying cation binding for other crown ether-based systems,[26] we decided to assess the binding affinities of **1** toward Na^+, Mg^{2+}, K^+, and Ca^{2+} through ^1H NMR titration experiments at 37 °C. Addition of Na^+ or Mg^{2+} to solutions of **1** in D_2O resulted in downfield shifting of ^1H NMR resonances. The resonances shifted non-linearly with increasing concentrations of Na^+ or Mg^{2+}, suggesting the presence of equilibrium (see Figures 3, left, and S3–S5). The changes in chemical shift for the peaks at ca. 202 and 123 ppm were most pronounced and could be modeled[27] to provide average dissociation constants of K_d = 4.8(3) and 23(2) mM for $[LCoNa]^+$ and $[LCoMg]^{2+}$, respectively (see Figures 3, left, and S3–S9, and Table S4). Owing to the structural similarity between 18-crown-6 and the crown ether moiety of H_2L, **1** was expected to display higher affinity toward K^+ than toward the smaller ions Na^+ and Mg^{2+}.[18,29] As such, Na^+ was introduced to compete with K^+ for binding to LCo, so an equilibrium could be established at a concentration of **1** high enough to be observed by ^1H NMR. A similar non-linear shift of ^1H resonances was observed upon incremental addition of KNO_3 to a D_2O solution of **1** containing 150 mM of $NaNO_3$ as observed in the Na^+ and Mg^{2+} titration experiments, albeit less pronounced (see Figures S10 and S11). A fit of the data gave an average value of K_d = 0.3(2) mM for $[LCoK]^+$ (see Figures S12 and S13, and Table S4).

For the NMR titrations of LCo with Na^+, Mg^{2+}, and K^+, only one set of ^1H resonances was observed in each case, indicating fast cation exchange rates compared to the ^1H NMR acquisition time scale (ca. 10^{-3} s). In contrast, when Ca^{2+} was added to a D_2O solution of **1** containing K^+ as a competing ion, two sets of ^1H resonances were observed (see Figure 3, right). This observation suggests a slow cation exchange between $[LCoK]^+$ and $[LCoCa]^{2+}$ in aqueous solutions. Integrations of the peaks at 207 and 245 ppm, corresponding to $[LCoK]^+$ and $[LCoCa]^{2+}$, respectively, could be employed to derive the mole fraction of $[LCoCa]^{2+}$ as a function of $[Ca^{2+}]$ (see

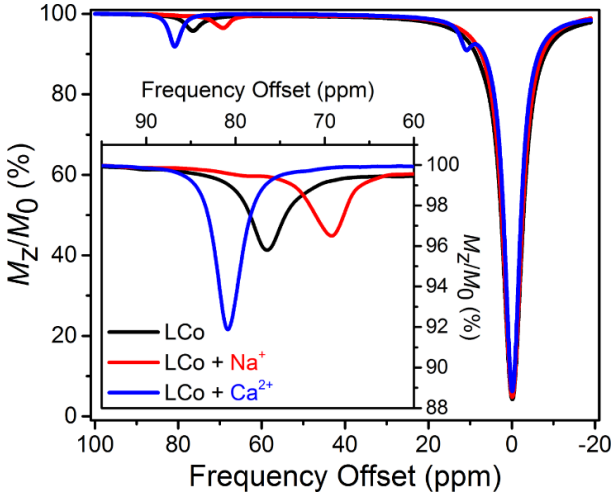

Figure 4. CEST spectra collected at 11.7 T and 37 °C using a 3 s presaturation pulse and B_1 = 21 μT for 5 mM aqueous solutions of **1** containing 50 mM of HEPES buffered at pH 7.4 (black), and with 15 mM of Na^+ (red) or Ca^{2+} (blue). Inset: Expanded view of relevant CEST peaks.

Figure S14). By using the previously determined K_d value for $[LCoK]^+$ and $[Ca^{2+}]$ at 50% $[LCoCa]^{2+}$ formation, a value of K_d = 0.01(1) mM was estimated for $[LCoCa]^{2+}$ (see equation 3). Average values of K_d for the different cation-bound complexes of **1** are summarized in Table 2. Cation affinity for **1** follows the order $Ca^{2+} > K^+ > Na^+ > Mg^{2+}$. The tightest binding of **1** to Ca^{2+} is likely a result of an optimal ionic radius in conjunction with a high positive charge. Most importantly, these K_d values suggest that **1** will near exclusively bind Ca^{2+} and Na^+ over Mg^{2+} and K^+ under physiological conditions owing to low affinities and/or low concentrations of the latter two ions. Furthermore, similar values of K_d = 1.8(9)–3.7(9) mM were obtained for $[LCoNa]^+$ in HEPES solutions buffered at pH 7.3–7.5 as observed in D_2O (see Figures S15–S17 and Table S5), indicating that ion binding to **1** is minimally affected by pH in the physiological range.

CEST Properties. To investigate the potential of **1** as a cation-responsive PARACEST probe, CEST spectra were collected at 37 °C for solutions containing 5 mM of **1** and 50 mM of HEPES buffered at pH 7.4, in the absence and presence of 15 mM of Na^+ or Ca^{2+}. For solutions of **1**, $[LCoNa]^+$, and $[LCoCa]^{2+}$, CEST peaks were observed at 77, 69, and 80 ppm, respectively, with 4.8, 3.9, and 8.5% H_2O signal reduction, respectively (see Figure 4). These CEST peak frequencies are consistent with the assignment of carboxamide resonances from the ^1H NMR spectra. Despite the low signal intensities, the frequency difference between the three CEST peaks highlights the effectiveness of LCo to distinguish between Na^+ and Ca^{2+} in solution. A second CEST peak was observed at 11 ppm in the spectrum for $[LCoCa]^{2+}$, likely stemming from a coordinating H_2O molecule. Exchange rates for the carboxamide protons were estimated by the Omega plot method at 37 °C and pH 7.4.[25] Rate constants of k_{ex} = 4.0(5) × 10^2, 3.0(6) × 10^2, and 2.4(2) × 10^2 s^{-1} were obtained for **1**, $[LCoNa]^+$, and $[LCoCa]^{2+}$, respectively, (see Figure S19). These values are in good agreement with those reported for other carboxamide-based PARACEST agents.[9,10c,11a,c,h–k] The stronger CEST effect observed for $[LCoCa]^{2+}$ compared to that for $[LCoNa]^+$, despite similar values of k_{ex} for the two complexes, could be due to the presence of a third pool of labile protons from the coordinating H_2O molecule in HEPES buffer solutions of $[LCoCa]^{2+}$. This hypothesis is supported by the observation of an additional peak at 11 ppm in the CEST spectrum for $[LCoCa]^{2+}$.

Quantitation of Ca^{2+} Concentration in Aqueous Solutions. To evaluate the ability of **1** to enable a ratiometric quantitation of the

concentration of Ca^{2+} under physiological conditions, CEST spectra were collected at 37 °C for a solution containing 2.0 mM of **1**, 150 mM of NaCl, and 50 mM of HEPES buffered at pH 7.4, upon incremental addition of $Ca(NO_3)_2$. In the absence of Ca^{2+}, a single CEST peak at 69 ppm was observed, indicating complete formation of $[LCoNa]^+$. However, upon addition of Ca^{2+}, a new peak appeared at 80 ppm, corresponding to $[LCoCa]^{2+}$. The intensity of this peak increased monotonically until reaching saturation at $[Ca^{2+}]$ = 3.13 mM. Due to partial overlap with the peak at 80 ppm, the CEST peak intensity at 69 ppm first increased until $[Ca^{2+}]$ = 1.00 mM, but then decreased substantially with increasing $[Ca^{2+}]$, reaching a value of less than 1% at $[Ca^{2+}]$ = 3.13 mM (see Figure 5, upper). The appearance of the CEST peak at 80 ppm demonstrates that **1** selectively binds Ca^{2+} over Na^+ under physiological conditions.[14] Importantly, the intensity of the $[LCoCa]^{2+}$ CEST peak at 80 ppm reached saturation at $[Ca^{2+}]$ = 3.13 mM rather than 2.00 mM, indicating that cation selectivity is modest enough to allow for an equilibrium between $[LCoNa]^+$ and $[LCoCa]^{2+}$, thus enabling ratiometric quantitation of $[Ca^{2+}]$. These observations are consistent with the K_d values estimated for the two complexes.

To assess the influence of probe concentration on the CEST properties of **1**, variable-$[Ca^{2+}]$ CEST spectra were collected for various concentrations of **1** in analogy to the 2.0 mM sample (see Figures S20–S22). The intensities of the CEST peaks at 80 and 69 ppm changed considerably as the concentration of **1** was varied, demonstrating the shortcoming of detecting $[Ca^{2+}]$ solely based on CEST peak intensities. However, the ratio of peak intensities at 80 and 69 ppm ($CEST_{80\ ppm}/CEST_{69\ ppm}$) was only minimally affected by the concentration of **1** (see Figure 5, lower). Note that the CEST effect at 69 ppm cannot be accurately determined when $[Ca^{2+}] > 3$ mM owing to the low intensity (see Figure 5, upper). As such, $CEST_{80\ ppm}/CEST_{69\ ppm}$ values for $[Ca^{2+}] > 3$ mM may contain significant error. The correlation between $CEST_{80\ ppm}/CEST_{69\ ppm}$ and $[Ca^{2+}]$ for $[Ca^{2+}] < 3$ mM can be fitted using the following empirical exponential model:

$$CEST_{80\ ppm}/CEST_{69\ ppm} = \exp([Ca^{2+}] - x) \quad (4)$$

Fits of the CEST data to equation 4 afforded x = 0.92(4), 0.90(6), 1.6(1), and 2.8(2) for 2.0, 2.8, 5.6, and 11 mM of **1**, respectively. Therefore, when only data for $[Ca^{2+}] < 3$ mM are examined, the equations for 2.0 and 2.8 mM of **1** are statistically indistinguishable (see Figure 5, lower, inset). However, the equations for 5.6 and 11 mM of **1** are significantly different, suggesting that $[LCoNa]^+$ and $[LCoCa]^{2+}$ are not in equilibrium at higher concentrations of **1** (≥ 5.6 mM), likely due to strong Ca^{2+} binding. These results establish the validity of using the CEST peak intensity ratio to quantitate $[Ca^{2+}]$ independent of the concentration of **1** within a regime where the concentration of **1** is sufficiently low (< 3 mM) to allow for an equilibrium between $[LCoNa]^+$ and $[LCoCa]^{2+}$. Accordingly, to expand the range of concentration-independent quantitation of $[Ca^{2+}]$ using PARACEST, the probe should exhibit weaker binding affinity toward Ca^{2+} and stronger CEST effects.

To further test the feasibility of **1** to quantitate $[Ca^{2+}]$ in physiological environments, variable-$[Ca^{2+}]$ CEST experiments were carried out at 37 °C for a pH 7.4 buffer solution containing 2.8 mM of **1**, 150 mM of Na^+, 4 mM of K^+, and 0.2 mM of Mg^{2+} to mimic their physiological concentrations[14] (see Figure S23). Prior to addition of Ca^{2+}, a single CEST peak at 69 ppm was observed with 0.8% CEST effect, suggesting that LCo exclusively bound Na^+. Upon incremental addition of Ca^{2+}, the intensity of this peak first increased to 4% at $[Ca^{2+}]$ = 1.01 mM and then decreased monotonically with increasing $[Ca^{2+}]$, whereas a CEST signal at 80 ppm corresponding to $[LCoCa]^{2+}$ appeared and reached a maximum intensity of 6.5% at $[Ca^{2+}]$ = 3.40 mM. These spectral changes are analogous to those observed in the absence of K^+ and Mg^{2+}. An equilibrium between $[LCoCa]^{2+}$ and $[LCoNa]^+$ was again established, as the CEST peak at 80 ppm reached a maximum intensity at $[Ca^{2+}] > 2.8$ mM. However, both CEST peaks were noticeably broader compared to those

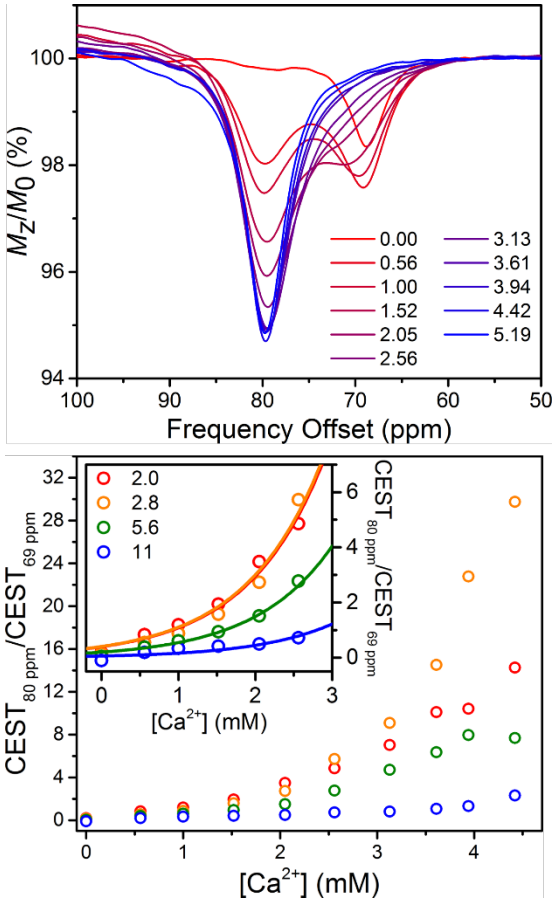

Figure 5. Upper: CEST spectra collected at 11.7 T and 37 °C using a 3 s presaturation pulse and B_1 = 21 μT for 50 mM HEPES buffer solutions containing 2.0 mM of **1** and 150 mM of NaCl at pH 7.4 with increasing $[Ca^{2+}]$. The legend denotes $[Ca^{2+}]$ (mM). Lower: Ratio of CEST peak intensities from presaturation at 80 and 69 ppm vs $[Ca^{2+}]$. Inset: Expanded view of the relevant data. Circles and solid lines represent experimental data and fits, respectively. The legend denotes [**1**] (mM).

observed in the absence of K^+ and Mg^{2+}. Specifically, the two peaks start to coalesce at $[Ca^{2+}] > 1$ mM, as evidenced by the downfield and upfield shifting of the CEST peaks at 69 and 80 ppm, respectively. Together, these observations suggest an accelerated cation exchange between $[LCoCa]^{2+}$ and $[LCoNa]^+$, likely stemming from the presence of K^+ and Mg^{2+}.

The plot of $CEST_{80\ ppm}/CEST_{69\ ppm}$ vs $[Ca^{2+}]$, as depicted in Figure S24, reveals that $CEST_{80\ ppm}/CEST_{69\ ppm}$ increases with increasing $[Ca^{2+}]$, following a similar trend as the data shown in Figure 5, lower. Fits of the data to equation 4 using $[Ca^{2+}] < 2.5$ mM gave x = 1.56(8) (see Figure S25), which is significantly higher than the value of x = 0.90(6) obtained for the 2.8 mM sample of **1** in the absence of K^+ and Mg^{2+}. This discrepancy can likely be attributed to the increased cation exchange rate between $[LCoCa]^{2+}$ and $[LCoNa]^+$ in the presence of K^+ and Mg^{2+}. Note that the empirical exponential model provided in equation 4 does not fit the $CEST_{80\ ppm}/CEST_{69\ ppm}$ vs $[Ca^{2+}]$ data for the physiological ion mixture very well. However, an alternative exponential model given in equation 5 affords much better agreement, providing parameters of a = 0.38(6) and b = 0.73(7) (see Figure S26).

$$CEST_{80\ ppm}/CEST_{69\ ppm} = a \times \exp(b \times [Ca^{2+}]) \quad (5)$$

Taken together, variable-$[Ca^{2+}]$ CEST experiments for solutions of **1** with different cations confirm that **1** selectively and reversibly binds Ca^{2+} and Na^+ over the related cations K^+ and Mg^{2+}, verifying the feasibility of ratiometric quantitation of $[Ca^{2+}]$ under physiological conditions.[14] While interference from binding other cations

is insignificant, the rate of cation exchange was found to influence the CEST peak intensity ratio, highlighting the necessity of constructing a calibration curve under conditions that strongly resemble the targeted environment. As such, the effects of cation exchange rates on the CEST properties of different cation-bound probes should be strongly considered in the design of future cation-responsive CEST probes.

Stability Studies. Finally, we sought to investigate the stability of **1** in aqueous solutions. Cyclic voltammetry experiments were carried out for solutions of **1** with 50 mM of HEPES buffered at pH 7.4 in the absence and presence of a mixture of Na^+, K^+, Mg^{2+}, and Ca^{2+} ions at their physiological concentrations.[14] In the absence of the inorganic cations, **1** exhibits one pseudo-reversible redox process at 440 mV vs NHE that is assigned to the $Co^{II/III}$ potential (see Figure S27). Surprisingly, the pseudo-reversible $Co^{II/III}$ redox event was shifted cathodically to 374 mV vs NHE in the presence of the cation mixture (see Figure S28). The more reductive potential observed in the presence of the inorganic cations could be attributed to the different electrolytes in the sample solutions. Nevertheless, both potentials are more reductive than that for the reduction of O_2 to H_2O in a neutral solution,[28] suggesting that **1** is susceptible to oxidation in air. To further study the stability of **1** under aerobic conditions, a solution of **1** buffered at pH 7.4 was prepared under dinitrogen atmosphere and exposed to air while a UV-visible absorption spectrum was recorded at regular intervals (see Figure S29). Over a 24 h period, the intensities of the absorption bands centered at 247 and 296 nm gradually decreased, likely corresponding to the oxidation of Co^{2+} to Co^{3+} over the course of hours.

CONCLUSIONS AND OUTLOOK

The foregoing results demonstrate the feasibility of quantitating Ca^{2+} concentration in a ratiometric manner through cation-dependent CEST effects. Importantly, the LCo probe features both a selective and a reversible binding of Ca^{2+} and Na^+ in the presence of similar cations. The CEST peaks for the Ca^{2+}- and Na^+-bound probes are highly shifted and can be distinctively addressed, thanks to the sensitivity of ^1H NMR hyperfine shift and magnetic anisotropy to changes in the coordination environment at the paramagnetic Co^{II} center. Moreover, variable-[Ca^{2+}] CEST experiments confirmed the ability of LCo to quantitate [Ca^{2+}], independent of the probe concentration when an equilibrium between [$LCoCa^{2+}$] and [$LCoNa^+$] was achieved ([LCo] < 3 mM and [Ca^{2+}] < 3 mM).

The current proof-of-principle study represents a first step toward practical quantitation of [Ca^{2+}], and potentially other physiologically relevant cations, in a concentration-independent manner. While the weak CEST effects and air-sensitivity may preclude the practical use of the current LCo probe, we have established that the combination of magnetic anisotropy modulation and cation recognition by a crown ether moiety is a promising cation-sensing strategy. Future efforts will be directed toward tuning the transition metal and pendent CEST-active groups to optimize sensitivity, cation binding affinities, CEST peak intensities, and probe stability, as well as modifying the crown ether unit toward sensing cations of different sizes.

ASSOCIATED CONTENT

Supporting Information

The Supporting Information is available free of charge on the ACS Publications website.

Additional experimental details and characterization data (PDF)

Crystallographic data for **1′**, **2′**, and **3′** (CIF)

AUTHOR INFORMATION

Corresponding Author

dharris@northwestern.edu

ORCID

Kang Du: 0000-0001-9947-2320

Agnes E. Thorarinsdottir: 0000-0001-9378-4454

T. David Harris: 0000-0003-4144-900x

Notes

The authors declare no competing financial interest.

ACKNOWLEDGMENTS

This research was funded by the Air Force Research Laboratory under agreement no. FA8659-15-2-5518 and Northwestern University.

REFERENCES

(1) (a) Coleman, R. E. Metastatic Bone Disease: Clinical Features, Pathophysiology and Treatment Strategies. *Cancer Treat. Rev.* **2001**, *27*, 165–176. (b) Mundy, G. R. Metastasis to Bone: Causes, Consequences and Therapeutic Opportunities. *Nat. Rev. Cancer* **2002**, *2*, 584–593. (c) Kyle, R. A.; Rajkumar, S. V. Multiple Myeloma. *N. Engl. J. Med.* **2004**, *351*, 1860–1873.

(2) (a) Fraser, W. D. Hyperparathyroidism. *Lancet* **2009**, *374*, 145–158. (b) Blaine, J.; Chonchol, M.; Levi, M. Renal Control of Calcium, Phosphate, and Magnesium Homeostasis. *Clin. J. Am. Soc. Nephrol.* **2015**, *10*, 1257–1272.

(3) (a) Ralston, S. H. Paget's Disease of Bone. *N. Engl. J. Med.* **2013**, *368*, 644–650. (b) Tuck, S. P.; Layfield, R.; Walker, J.; Mekkayil, B.; Francis, R. Adult Paget's Disease of Bone: A Review. *Rheumatology* **2017**, *56*, 2050–2059.

(4) Minisola, S.; Pepe, J.; Piemonte, S.; Cipriani, C. The Diagnosis and Management of Hypercalcaemia. *BMJ* **2015**, *350*, h2723.

(5) Ziegler, R. Hypercalcemic Crisis. *J. Am. Soc. Nephrol.* **2001**, *12*, S3–S9.

(6) (a) Lauffer, R. B. Paramagnetic Metal Complexes as Water Proton Relaxation Agents for NMR Imaging: Theory and Design. *Chem. Rev.* **1987**, *87*, 901–927. (b) Caravan, P.; Ellison, J. J.; McMurry, T. J.; Lauffer, R. B. Gadolinium(III) Chelates as MRI Contrast Agents: Structure, Dynamics, and Applications. *Chem. Rev.* **1999**, *99*, 2293–2352. (c) Caravan, P. Strategies for Increasing the Sensitivity of Gadolinium Based MRI Contrast Agents. *Chem. Soc. Rev.* **2006**, *35*, 512–523.

(7) (a) Li, W.; Fraser, S. E.; Meade, T. J. A Calcium-Sensitive Magnetic Resonance Imaging Contrast Agent. *J. Am. Chem. Soc.* **1999**, *121*, 1413–1414. (b) Li, W.; Parigi, G.; Fragai, M.; Luchinat, C.; Meade, T. J. Mechanistic Studies of a Calcium-Dependent MRI Contrast Agent. *Inorg. Chem.* **2002**, *41*, 4018–4024. (c) Atanasijevic, T.; Shusteff, M.; Fam, P.; Jasanoff, A. Calcium-Sensitive MRI Contrast Agents Based on Superparamagnetic Iron Oxide Nanoparticles and Calmodulin. *Proc. Natl. Acad. Sci. U. S. A.* **2006**, *103*, 14707–14712. (d) Mishra, A.; Fousková, P.; Angelovski, G.; Balogh, E.; Mishra, A. K.; Logothetis, N. K.; Tóth, É. Facile Synthesis and Relaxation Properties of Novel Bispolyazamacrocyclic Gd^{3+} Complexes: An Attempt towards Calcium-Sensitive MRI Contrast Agents. *Inorg. Chem.* **2008**, *47*, 1370–1381. (e) Dhingra, K.; Maier, M. E.; Beyerlein, M.; Angelovski, G.; Logothetis, N. K. Synthesis and Characterization of a Smart Contrast Agent Sensitive to Calcium. *Chem. Commun.* **2008**, *0*, 3444–3446. (f) Angelovski, G.; Fousková, P.; Mamedov, I.; Canals, S.; Tóth, É.; Logothetis, N. K. Smart Magnetic Resonance Imaging Agents that Sense Extracellular Calcium Fluctuations. *ChemBioChem* **2008**, *9*, 1729–1734. (g) Que, E. L.; Chang, C. J. Responsive Magnetic Resonance Imaging Contrast Agents as Chemical Sensors for Metals in Biology and Medicine. *Chem. Soc. Rev.* **2010**, *39*, 51–60. (h) Mamedov, I.; Canals, S.; Henig, J.; Beyerlein, M.; Murayama, Y.; Mayer, H. A.; Logothetis, N. K.; Angelovski, G. In Vivo Characterization of a Smart MRI Agent That Displays an Inverse Response to Calcium Concentration. *ACS Chem. Neurosci.* **2010**, *1*, 819–828. (i) Heffern, M. C.; Matosziuk, L. M.; Meade, T. J. Lanthanide Probes for Bioresponsive Imaging. *Chem. Rev.* **2014**, *114*, 4496–4539. (j) Kadjane, P.; Platas-Iglesias, C.; Boehm-Sturm, P.; Truffault, V.; Hagberg, G. E.; Hoehn, M.; Logothetis, N. K.; Angelovski, G. Dual-Frequency Calcium-Responsive MRI Agents. *Chem. Eur. J.* **2014**, *20*, 7351–7362. (k) MacRenaris, K. W.; Ma, Z.; Krueger, R. L.; Carney, C. E.; Meade, T. J. Cell-

Permeable Esterase-Activated Ca(II)-Sensitive MRI Contrast Agent. *Bioconjugate Chem.* **2016**, *27*, 465–473.
(8) Selected references: (a) Zhang, S.; Michaudet, L.; Burgess, S.; Sherry, A. D. The Amide Protons of an Ytterbium(III) Dota Tetraamide Complex Act as Efficient Antennae for Transfer of Magnetization to Bulk Water. *Angew. Chem., Int. Ed.* **2002**, *41*, 1919–1921. (b) Aime, S.; Delli Castelli, D.; Terreno, E. Novel pH-Reporter MRI Contrast Agents. *Angew. Chem., Int. Ed.* **2002**, *41*, 4334–4336. (c) Terreno, E.; Delli Castelli, D.; Cravotto, G.; Milone, L.; Aime, S. Ln(III)-DOTAMGly Complexes: A Versatile Series to Access the Determinants of the Efficacy of Paramagnetic Chemical Exchange Saturation Transfer Agents for Magnetic Resonance Imaging Applications. *Invest. Radiol.* **2004**, *39*, 235–243. (d) Woods, M.; Woessner, D. E.; Zhao, P.; Pasha, A.; Yang, M.-Y.; Huang, C.-H.; Vasalitiy, O.; Morrow, J. R.; Sherry, A. D. Europium(III) Macrocyclic Complexes with Alcohol Pendant Groups as Chemical Exchange Saturation Transfer Agents. *J. Am. Chem. Soc.* **2006**, *128*, 10155–10162. (e) Angelovski, G.; Chauvin, T.; Pohmann, R.; Logothetis, N. K.; Tóth, É. Calcium-Responsive Paramagnetic CEST Agents. *Bioorg. Med. Chem.* **2011**, *19*, 1097–1105.
(9) Selected references: (a) Dorazio, S. J.; Tsitovich, P. B.; Siters, K. E.; Spernyak, J. A.; Morrow, J. R. Iron(II) PARACEST MRI Contrast Agents. *J. Am. Chem. Soc.* **2011**, *133*, 14154–14156. (b) Tsitovich, P. B.; Morrow, J. R. Macrocyclic Ligands for Fe(II) ParaCEST and Chemical Shift MRI Contrast Agents. *Inorg. Chim. Acta* **2012**, *393*, 3–11. (c) Olatunde, A. O.; Dorazio, S. J.; Spernyak, J. A.; Morrow, J. R. The NiCEST Approach: Nickel(II) ParaCEST MRI Contrast Agents. *J. Am. Chem. Soc.* **2012**, *134*, 18503–18505. (d) Dorazio, S. J.; Morrow, J. R. Iron(II) Complexes Containing Octadentate Tetraazamacrocycles as ParaCEST Magnetic Resonance Imaging Contrast Agents. *Inorg. Chem.* **2012**, *51*, 7448–7450. (e) Dorazio, S. J.; Olatunde, A. O.; Spernyak, J. A.; Morrow, J. R. CoCEST: Cobalt(II) Amide-Appended ParaCEST MRI Contrast Agents. *Chem. Commun.* **2013**, *49*, 10025–10027. (f) Du, K.; Harris, T. D. A Cu^{II}_2 Paramagnetic Chemical Exchange Saturation Transfer Contrast Agent Enabled by Magnetic Exchange Coupling. *J. Am. Chem. Soc.* **2016**, *138*, 7804–7807.
(10) (a) Tsitovich, P. B.; Spernyak, J. A.; Morrow, J. R. A Redox-Activated MRI Contrast Agent That Switches Between Paramagnetic and Diamagnetic States. *Angew. Chem., Int. Ed.* **2013**, *52*, 13997–14000. (b) Tsitovich, P. B.; Burns, P. J.; McKay, A. M.; Morrow, J. R. Redox-Activated MRI Contrast Agents Based on Lanthanide and Transition Metal Ions. *J. Inorg. Biochem.* **2014**, *133*, 143–154. (c) Du, K.; Waters, E. A.; Harris, T. D. Ratiometric Quantitation of Redox Status with a Molecular Fe_2 Magnetic Resonance Probe. *Chem. Sci.* **2017**, *8*, 4424–4430.
(11) (a) Liu, G.; Li, Y.; Sheth, V. R.; Pagel, M. D. Imaging in Vivo Extracellular pH with a Single Paramagnetic Chemical Exchange Saturation Transfer Magnetic Resonance Imaging Contrast Agent. *Mol. Imaging* **2012**, *11*, 47–57. (b) Sheth, V. R.; Li, Y.; Chen, L. Q.; Howison, C. M.; Flask, C. A.; Pagel, M. D. Measuring in Vivo Tumor pHe with CEST-FISP MRI. *Magn. Reson. Med.* **2012**, *67*, 760–768. (c) McVicar, N.; Li, A. X.; Suchý, M.; Hudson, R. H. E.; Menon, R. S.; Bartha, R. Simultaneous in Vivo pH and Temperature Mapping Using a PARACEST-MRI Contrast Agent. *Magn. Reson. Med.* **2013**, *70*, 1016–1025. (d) Delli Castelli, D.; Ferrauto, G.; Cutrin, J. C.; Terreno, E.; Aime, S. In Vivo Maps of Extracellular pH in Murine Melanoma by CEST-MRI. *Magn. Reson. Med.* **2014**, *71*, 326–332. (e) Rancan, G.; Delli Castelli, D.; Aime, S. MRI CEST at 1T with Large μ_{eff} Ln^{3+} Complexes Tm^{3+}-HPDO3A: An Efficient MRI pH Reporter. *Magn. Reson. Med.* **2016**, *75*, 329–336. (f) Wu, Y.; Zhang, S.; Soesbe, T. C.; Yu, J.; Vinogradov, E.; Lenkinski, R. E.; Sherry, A. D. pH Imaging of Mouse Kidneys in Vivo Using a Frequency-Dependent ParaCEST Agent. *Magn. Reson. Med.* **2016**, *75*, 2432–2441. (g) Tsitovich, P. B.; Cox, J. M.; Spernyak, J. A.; Morrow, J. R. Gear Up for a pH Shift: A Responsive Iron(II) 2-Amino-6-Picolyl-Appended Macrocyclic ParaCEST Agent That Protonates at a Pendent Group. *Inorg. Chem.* **2016**, *55*, 12001–12010. (h) Thorarinsdottir, A. E.; Du, K.; Collins, J. H. P.; Harris, T. D. Ratiometric pH Imaging with a Co^{II}_2 MRI Probe via CEST Effects of Opposing pH Dependences. *J. Am. Chem. Soc.* **2017**, *139*, 15836–15847. (i) Srivastava, K.; Ferrauto, G.; Young, V. G.; Aime, S.; Pierre, V. C. Eight-Coordinate, Stable Fe(II) Complex as a Dual ^{19}F and CEST Contrast Agent for Ratiometric pH Imaging. *Inorg. Chem.* **2017**, *56*, 12206–12213. (j) Thorarinsdottir, A. E.; Tatro, S. M.; Harris, T. D. Electronic Effects of Ligand Substitution in a Family of Co^{II}_2 PARACEST pH Probes. *Inorg. Chem.* **2018**, *57*, 11252–11263. (k) Thorarinsdottir, A. E.; Harris, T. D. Dramatic Enhancement in pH Sensitivity and Signal Intensity through Ligand Modification of a Dicobalt PARACEST Probe. *Chem. Commun.* **2019**, *55*, 794–797.
(12) (a) Zhang, S.; Malloy, C. R.; Sherry, A. D. MRI Thermometry Based on PARACEST Agents. *J. Am. Chem. Soc.* **2005**, *127*, 17572–17573. (b) Li, A. X.; Wojciechowski, F.; Suchý, M.; Jones, C. K.; Hudson, R. H. E.; Menon, R. S.; Bartha, R. A Sensitive PARACEST Contrast Agent for Temperature MRI: Eu^{3+}-DOTAM-Glycine(Gly)-Phenylalanine(Phe). *Magn. Reson. Med.* **2008**, *59*, 374–381. (c) Delli Castelli, D.; Terreno, E.; Aime, S. Yb(III)-HPDO3A: A Dual pH- and Temperature-Responsive CEST Agent. *Angew. Chem., Int. Ed.* **2011**, *50*, 1798–1800. (d) Jeon, I.-R.; Park, J. G.; Haney, C. R.; Harris, T. D. Spin Crossover Iron(II) Complexes as PARACEST MRI Thermometers. *Chem. Sci.* **2014**, *5*, 2461–2465.
(13) (a) Trokowski, R.; Ren, J.; Kálmán, F. K.; Sherry, A. D. Selective Sensing of Zinc Ions with a PARACEST Contrast Agent. *Angew. Chem., Int. Ed.* **2005**, *44*, 6920–6923. (b) Srivastava, K.; Ferrauto, G.; Harris, S. M.; Longo, D. L.; Botta, M.; Aime, S.; Pierre, V. C. Complete On/Off Responsive ParaCEST MRI Contrast Agents for Copper and Zinc. *Dalton Trans.* **2018**, *47*, 11346–11357.
(14) (a) Wan, Q. J.; Kubáň, P.; Tanyanyiwa, J.; Rainelli, A.; Hauser, P. C. Determination of Major Inorganic Ions in Blood Serum and Urine by Capillary Electrophoresis with Contactless Conductivity Detection. *Anal. Chim. Acta* **2004**, *525*, 11–16. (b) Le, T.; Bhushan, V.; Sochat, M.; Chavda, Y.; Zureick, A.; Kalani, M.; Kallianos, K. *First Aid for the USMLE Step 1: 2018 a Student-to-Student Guide*, 28th ed.; McGraw-Hill Education: New York, 2017.
(15) Bar-Shir, A.; Gilad, A. A.; Chan, K. W. Y.; Liu, G.; van Zijl, P. C. M.; Bulte, J. W. M.; McMahon, M. T. Metal Ion Sensing Using Ion Chemical Exchange Saturation Transfer ^{19}F Magnetic Resonance Imaging. *J. Am. Chem. Soc.* **2013**, *135*, 12164–12167.
(16) (a) van Staveren, C. J.; van Eerden, J.; van Veggel, F. C. J. M.; Harkema, S.; Reinhoudt, D. N. Cocomplexation of Neutral Guests and Electrophilic Metal Cations in Synthetic Macrocyclic Hosts. *J. Am. Chem. Soc.* **1988**, *110*, 4994–5008. (b) Caneschi, A.; Sorace, L.; Casellato, U.; Tomasin, P.; Vigato, P. A. d- or f-Mononuclear and Related Heterodinuclear Complexes with [1+1] Asymmetric Compartmental Macrocycles. *Eur. J. Inorg. Chem.* **2004**, 3887–3900. (c) Pierre, V. C.; Harris, S. M.; Pailloux, S. L. Comparing Strategies in the Design of Responsive Contrast Agents for Magnetic Resonance Imaging: A Case Study with Copper and Zinc. *Acc. Chem. Res.* **2018**, *51*, 342–351.
(17) (a) Bertini, I.; Luchinat, C. *NMR of Paramagnetic Molecules in Biological Systems*; The Benjamin/Cummings Publishing Company, Inc.: Menlo Park, 1986. (b) Bertini, I.; Luchinat, C. The Hyperfine Shift. *Coord. Chem. Rev.* **1996**, *150*, 29–75. (c) Bertini, I.; Luchinat, C. Relaxation. *Coord. Chem. Rev.* **1996**, *150*, 77–110. (d) Bertini, I.; Luchinat, C.; Parigi, G. *Solution NMR of Paramagnetic Molecules: Applications to Metallobiomolecules and Models*; Elsevier Science B.V.: Amsterdam, 2001.
(18) Reath, A. H.; Ziller, J. W.; Tsay, C.; Ryan, A. J.; Yang, J. Y. Redox Potential and Electronic Structure Effects of Proximal Nonredox Active Cations in Cobalt Schiff Base Complexes. *Inorg. Chem.* **2017**, *56*, 3713–3718.
(19) *APEX2*, version. 2009.1; Bruker Analytical X-Ray Systems, Inc.: Madison, WI, 2009.
(20) Sheldrick, G. M. *SADABS*, version 2.03; Bruker Analytical X-ray Systems, Inc.: Madison, WI, 2000.
(21) (a) Sheldrick, G. M. *SHELXTL*, version 6.12; Bruker Analytical X-ray Systems, Inc.: Madison, WI, 2000. (b) Sheldrick, G. M. SHELXT–Integrated Space-Group and Crystal-Structure Determination. *Acta Crystallogr., Sect. A: Found. Adv.* **2015**, *71*, 3–8. (c) Dolomanov, O. V.; Bourhis, L. J.; Gildea, R. J.; Howard, J. A. K.; Puschmann, H. OLEX2: A Complete Structure Solution, Refinement and Analysis Program. *J. Appl. Crystallogr.* **2009**, *42*, 339–341.
(22) Chilton, N. F.; Anderson, R. P.; Turner, L. D.; Soncini, A.; Murray, K. S. PHI: A Powerful New Program for the Analysis of Anisotropic Monomeric and Exchange-Coupled Polynuclear d- and f-Block Complexes. *J. Comput. Chem.* **2013**, *34*, 1164–1175.
(23) (a) Evans, D. F. The Determination of the Paramagnetic Susceptibility of Substances in Solution by Nuclear Magnetic Resonance. *J. Chem. Soc.* **1959**, *0*, 2003–2005. (b) Schubert, E. M. Utilizing the Evans Method with a Superconducting NMR Spectrometer in the Undergraduate Laboratory. *J. Chem. Educ.* **1992**, *69*, 62.
(24) Bain, G. A.; Berry, J. F. Diamagnetic Corrections and Pascal's Constants. *J. Chem. Educ.* **2008**, *85*, 532–536.
(25) Dixon, W. T.; Ren, J.; Lubag, A. J. M.; Ratnakar, J.; Vinogradov, E.; Hancu, I.; Lenkinski, R. E.; Sherry, A. D. A Concentration-Independent Method to Measure Exchange Rates in PARACEST Agents. *Magn. Reson. Med.* **2010**, *63*, 625–632.
(26) (a) Hirose, K. A Practical Guide for the Determination of Binding Constants. *J. Incl. Phenom. Macrocycl. Chem.* **2001**, *39*, 193–209. (b) Ellis, A. L.; Mason, J. C.; Lee, H.-W.; Strekowski, L.; Patonay, G.; Choi, H.; Yang, J. J. Design, Synthesis, and Characterization of a Calcium-Sensitive Near Infrared Dye. *Talanta* **2002**, *56*, 1099–1107. (c) Reuter, K.; Buchner, M.

R.; Thiele, G.; von Hänisch, C. Stable Alkali-Metal Complexes of Hybrid Disila-Crown Ethers. *Inorg. Chem.* **2016**, *55*, 4441–4447. (d) Pauric, A. D.; Jin, S.; Fuller, T. J.; Balogh, M. P.; Halalay, I. C.; Goward, G. R. NMR Determination of the Relative Binding Affinity of Crown Ethers for Manganese Cations in Aprotic Nonaqueous Lithium Electrolyte Solutions. *J. Phys. Chem. C* **2016**, *120*, 3677–3683.

(27) Kuzmič, P. Program DYNAFIT for the Analysis of Enzyme Kinetic Data: Application to HIV Proteinase. *Anal. Biochem.* **1996**, *237*, 260–273.

(28) (a) Wood, P. M. The Potential Diagram for Oxygen at pH 7. *Biochem. J.* **1988**, *253*, 287−289. (b) Sawyer, D. T.; Sobkowiak, A.; Roberts, J. L. *Electrochemistry for Chemists*, 2nd ed.; John Wiley & Sons: New York, 1995.

(29) Chantarojsiri, T.; Ziller, J. W.; Yang, J. Y. Incorporation of Redox-Inactive Cations Promotes Iron Catalyzed Aerobic C–H Oxidation at Mild Potentials. *Chem. Sci.* **2018**, *9*, 2567–2574.

(30) Izatt, R. M.; Pawlak, K.; Bradshaw, J. S.; Bruening, R. L. Thermodynamic and Kinetic Data for Macrocycle Interactions with Cations and Anions. *Chem. Rev.* **1991**, *91*, 1721–2085.

(31) (a) Shannon, R. D. Revised Effective Ionic Radii and Systematic Studies of Interatomic Distances in Halides and Chalcogenides. *Acta Crystallogr., Sect. A* **1976**, *32*, 751–767. (b) Lang, P. F.; Smith, B. C. Ionic Radii for Group 1 and Group 2 Halide, Hydride, Fluoride, Oxide, Sulfide, Selenide and Telluride Crystals. *Dalton Trans.* **2010**, *39*, 7786–7791.

(32) Drew, M. G. B.; Harding, C. J.; McKee, V.; Morgan, G. G.; Nelson, J. Geometric Control of Manganese Redox State. *J. Chem. Soc., Chem. Commun.* **1995**, *0*, 1035–1038.

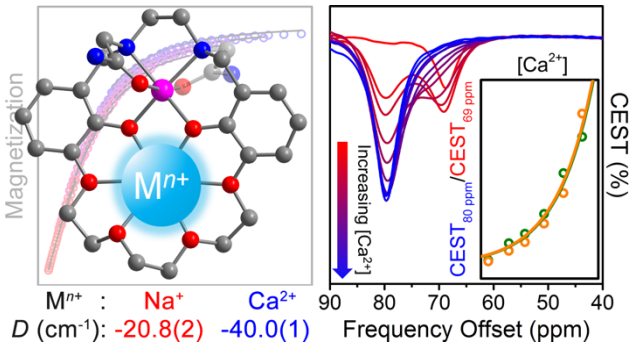
Magnetization
M^{n+}
M^{n+} : Na^+ Ca^{2+}
D (cm^{-1}): -20.8(2) -40.0(1)
Increasing [Ca^{2+}]
[Ca^{2+}]
$CEST_{80\ ppm}/CEST_{69\ ppm}$
CEST (%)
90 80 70 60 50 40
Frequency Offset (ppm)